BMC Oral Health

RESEARCH

Open Access

Mechanical and biological properties of 3D-printed porous titanium scaffolds coated with composite growth factors

Chunwen Jiang[1†], Guojia Gong[2†], Shan Xiao[1], Shengxiang Zhang[1], Diansheng Chen[1], Shuqing Song[3], Honglin Dai[1], Chongxue Wu[4], Qiaoru Zou[1], Jianping Li[5] and Bing Wen[1*]

Abstract

Background Osseointegration is considered a prerequisite for predicting implant success, and structure, biocompatibility, and properties of the implant are important parts of the factors that influence osseointegration. The focus of current research is on how to increase the strength of osseointegration on the implant and shorten the osseointegration time.

Methods In this research, different porous scaffolds, including uniform, radial-gradient, and axial-gradient porous, were designed and fabricated. Their mechanical properties and biocompatibility were comprehensively evaluated through mechanical tests and in vitro cellular experiments. A porous scaffold exhibiting optimal properties was identified through preliminary experiments. Subsequently, three different sets of composite scaffolds were developed, consisting of the selected scaffold modified with chitosan microspheres loaded with Bone Morphogenetic Protein-2 (BMP-2), Platelet-Derived Growth Factor-BB (PDGF-BB), or a combination of both. The biological responses to composite scaffolds were systematically examined through in vitro and in vivo experiments.

Results Finite element analysis indicated that the maximum equivalent stress of all three porous implants was lower than that of solid implants, while the maximum equivalent stress in the cortical bone of the porous group was higher than in the solid group. Compression tests confirmed that the elastic modulus of all three porous scaffold structures fall within the range of natural human bone. In vitro cell experiments showed that the radial gradient porous group scaffolds had the highest cell count and Alkaline phosphatase activity. The composite scaffolds exhibited superior wettability and water absorption properties compared to the non-coated scaffolds. Cell and animal experiments demonstrated that the titanium scaffolds co-modified with BMP-2 and PDGF-BB showed greater cell proliferation and new bone formation compared to scaffolds with single-factor coatings and uncoated scaffolds.

Conclusions Radial-gradient porous scaffolds exhibit compatible elastic modulus, excellent cell compatibility, and osteogenic potential, making them promising candidates for bone tissue engineering applications in dentistry. Furthermore, the composite scaffolds incorporating BMP-2 and PDGF-BB-loaded chitosan microspheres

†Chunwen Jiang and Guojia Gong contributed equally to this work.

*Correspondence:
Bing Wen
wenbing69@163.com

Full list of author information is available at the end of the article

demonstrated enhanced osteogenic differentiation compared to single-factor modified porous scaffolds, providing experimental evidence for the clinical application of novel implants.

Keywords Graded porous titanium scaffolds, 3D printing, BMP-2 and PDGF-BB, Mechanical properties, Biological performance, osteogenic-induced differentiation

Background

Ti alloys with lattice structures are garnering more and more attention in the field of bone repair or regeneration due to their superior structural, mechanical, and biological properties. The elastic modulus of Ti-6Al-4 V alloy (110 Gpa), which is commonly used in clinical practice, is much higher than that of human cortical bone (10–30 Gpa), and after long-term implantation, excessive micromovement of the implant-bone tissue and bacterial aggregation may occur due to the stress masking effect, which may induce peri-implantitis and ultimately loosen or even dislodge the implant [1–3]. The current research focuses on how to improve osseointegration strength and shorten the osseointegration time on implant surfaces. It has been found that three-dimensional composite porous implant surfaces are more conducive to the formation of osseointegration than conventional implants. The porous Ti scaffolds have a laminated porous structure similar to that of bone tissue and are structurally and mechanically similar to bone tissue, so by adjusting the parameters of pore shape, porosity, and pore diameter, the elastic modulus of the porous Ti scaffolds can be made to be close to that of natural bone [4–6]. Gradient porous Ti scaffolds not only address the insufficient strength of high-porosity Ti scaffolds with uniform pore sizes but also provide the spatial conditions necessary for osteoblast adhesion and proliferation. These scaffolds enhance osseointegration capability and exhibit excellent osteoconductivity [7, 8]. Recent investigations have explored the integration of Triply Periodic Minimal Surface (TPMS) structures into porous implant designs. Unlike geometric primitives (e.g., cylinders, cubes) with straight edges or sharp curvatures, TPMS structures exhibit bone-mimetic surface curvature and smoothness, creating superior biomorphic environments for cellular activities [9]. Moreover, as TPMS structures are mathematically defined, their dimensions and porosity gradient distributions can be precisely controlled through parametric modifications [10].Consequently, TPMS-based gradient structures demonstrate greater research potential than conventional lattice structures. Among TPMS architectures, the Gyroid structure has emerged as the predominant choice for biomedical applications, demonstrating exceptional biological compatibility and mechanical performance relative to other TPMS variants [11].

The ability of Three-dimensional (3D) printing technology to create implants with defined structures, shapes, and properties opens up the possibility of precise preparation of porous implants [12]. Among several 3D printing techniques, Selective laser melting (SLM) can precisely control the structure and distribution of pores during the preparation of porous materials, providing the most convenient technical support for the development of complex porous titanium [13].

Although 3D printing technology endows Ti6Al4V implants with excellent osteoconduction [14], the bioinert nature of the Ti6Al4V surface hinders precise control over osteoinduction [15]. Thus, enhancing the osteoinductive properties of 3D-printed porous Ti6Al4V remains crucial. The process of bone repair involves the participation of multiple growth factors, mainly including Bone Morphogenetic Protein-2 (BMP-2), BMP-4, and Platelet-Derived Growth Factor (PDGF). Bone morphogenetic proteins (BMP), a growth factor that has been widely used in bone defect repair, is a group of secreted multifunctional proteins that play an important role in bone and cartilage formation [16]. The main form of chitosan as a drug carrier is chitosan microspheres, which also possess biological activities such as antioxidant, bacteriostatic, and lipid-lowering [17]. Combination with drugs can enhance coating stability, maintain local drug concentration, and reduce bacterial aggrega PDGF is a dimeric cationic protein, of which PDGF-BB is the most active class, and it is a key regulator of tissue repair and regeneration [18]. Yoshida et al. [19]found in animal experiments that PDGF-BB promoted the migration of mesenchymal stem cells and osteoblasts into the artificial bone matrix material, after which these mesenchymal and osteoblasts could differentiate into osteoblasts. Fernandode [20] et al. have pointed out that the combination of biological agents, such as Recombinant Human Platelet-Derived Growth Factor-BB(rhPDGF-BB), with bone matrix materials could be a significant contribution to the regeneration of bone. An in vitro study showed that the combination of BMP-2 and PDGF-BB immobilized in heparin titanium enhanced osteoblast function compared to individual growth [21]. However, BMP-2 and PDGF-BB, with their significant bursts and short half-lives, are susceptible to short-term inactivation in vivo, thus affecting their osteoinductive capacity. Chitosan is often used as a carrier in combination with growth factors or antibiotics to build composite coatings for antimicrobial and slow-release effects [22].

During the implantation process, the implant will adhere and proliferate with the surrounding bone tissue, avoiding infection in the implantation area, enhancing

the adhesion between the implant and the surrounding bone tissue, and improving the success rate of the surgery [23]. The ionic gelation method employs the chemical reaction of non-toxic sodium Triphosphate (TPP) with chitosan to prepare chitosan nanoparticles [24]. Because of the easy operation of the ionic gel method, the obtained chitosan microspheres have a more uniform and stable particle size, and the method is easy to operate and mild reaction, especially suitable for the encapsulation of biologically active macromolecule drugs such as nucleic acids and proteins [25].

This study was designed to develop a novel implant capable of accelerating osteogenesis while enhancing osseointegration. The mechanical properties and in vitro biological performance of various gradient porous structures were systematically evaluated. Three types of TPMS-based porous scaffolds (uniform, radial, and axial gradient structures) were designed, with their mechanical properties characterized through finite element analysis and compression testing. In vitro assessment of cellular behavior was performed using rat bone marrow mesenchymal stem cells (rBMMSCs). To enhance bone integration, the optimal scaffold was modified by incorporating chitosan microspheres loaded with either BMP-2 or PDGF-BB. The effects of these composite scaffolds (incorporating either rhBMP-2 or PDGF-BB-loaded chitosan microspheres) on rBMMSC proliferation and differentiation were investigated, along with their osseointegration potential in vivo.

Materials and methods

Design and finite element analysis of the three-dimensional geometric model

The Gyroid structure, a representative TPMS architecture, was employed as the lattice unit (Fig. 1a). Porous scaffolds were designed in Rhinoceros 5.0 (Robert McNeel & Associates, USA) (Fig. 1b). Micro-CT scans (MILabs, Netherlands) of both the soft tissue-level implant and solid conical abutment (Baikant Medical, China) were exported as DICOM files and reconstructed in Siemens NX 1911 (Siemens PLM, Germany) to generate the implant model (Fig. 1c). The lattice structure was then Boolean operated with the implant model to create the final porous implant.

For finite element analysis, four implant models were established: solid (Co), uniform porosity (Un), radial-gradient (Gxy), and axial-gradient (Gz) porous structures (Fig. 1d-g). The porosity of the Un group was set at 50%, while the porosity distribution in the Gxy group gradually decreased from 70% at the periphery to 30% at the center. In the Gz group, the porosity distribution gradually declined from 70% at the bottom to 30% at the top. Subsequently, a mandibular model was constructed with dimensions of 25 mm in the mesiodistal direction and 15 mm in the buccal-lingual direction. The cortical bone thickness was set to 1.5 mm, with the inner cancellous bone surrounded by cortical bone [26]. The implant assembly was subsequently performed (Fig. 1h).

All materials were modeled as continuous, homogeneous, and isotropic elastic solids. Tetrahedral elements were utilized throughout the model to ensure computational accuracy, with a consistent element size of 0.3 mm maintained across all simulations. Material properties for the finite element analysis are provided in Table 1. Complete osseointegration was assumed, with perfect contact between implants and all bone structures (alveolar bone, cortical bone, and cancellous bone). For micromotion simulations, a friction coefficient of 0.3 was applied to allow for interfacial slip under loading conditions. Stress distributions were analyzed under both average and maximum occlusal loading conditions. First, a 120 N axial load was applied normally to the abutment surface. Second, an oblique load of 118.2 N was applied at 15° to the implant axis. This load was resolved into three orthogonal components: axial (114.6 N), bucco-lingual (17.1 N), and mesio-distal (23.4 N) [27].

Preparation and characterization of porous scaffolds

Different porous scaffold models were exported to STL format, and the FS271M metal 3D printer (Hunan Huashu High-Tech Co., China) was subsequently employed to fabricate the porous titanium alloy scaffold. The parameters of the SLM process used in 3D printing are presented in Table 2. The fabricated porous scaffolds underwent sequential ultrasonic cleaning in acetone, 75% ethanol, and deionized water for 1 h each. Following the cleaning process, the scaffolds were sterilized using high-temperature autoclaving at 120 °C for 30 min. After sterilization, the scaffolds were dried in an oven before further use.

The porous scaffolds for mechanical testing were designed as cylindrical structures with a diameter of 10 mm and a height of 20 mm (Fig. 2a, b). Porosity is defined as the ratio of the total volume occupied by void space within a porous scaffold. The porosity of the specimens was determined using the dry weight method. The porosity was calculated using Eq:

$$P = \left(1 - \frac{\rho_0}{\rho}\right) \times 100\% \qquad \rho_0 = m/V_0 \tag{1}$$

P represents the porosity of the porous scaffold. ρ_0 denotes the apparent density (g/cm^3), while ρ refers to the theoretical density of the porous titanium alloy scaffold material (4.5 g/cm^3). m represents the actual mass of the porous titanium alloy scaffold (g), and V_0 denotes its volume in the natural state (cm^3).

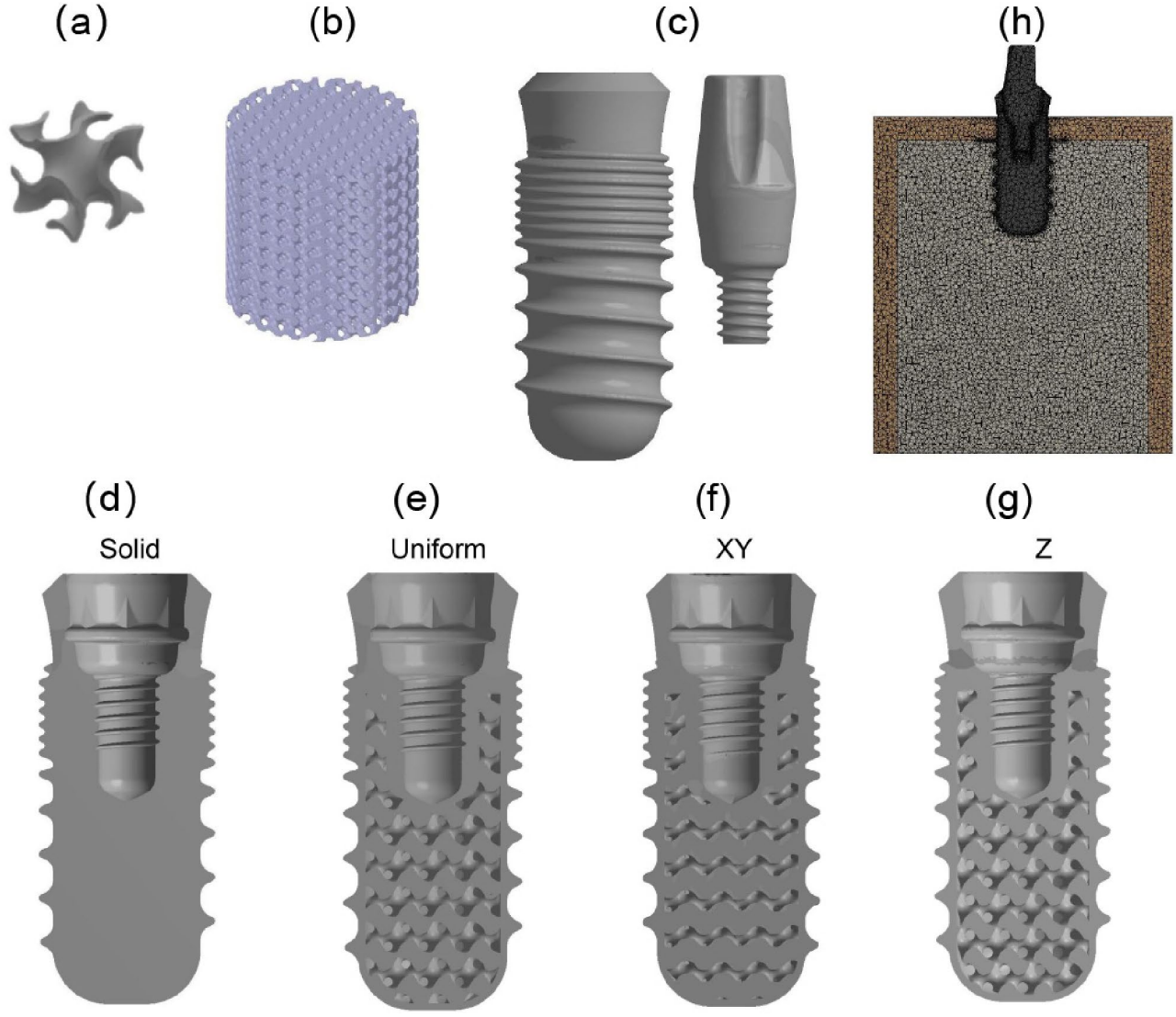

Fig. 1 3D geometric modeling of porous structures and FEA. **(a)** TPMS-based porous structures. **(b)** CAD model of the cylindrical porous scaffold. **(c)** Primitive dental implant with a solid conical abutting stage. Vertical section views of solid and porous dental implant models: **(d)** Co group, **(e)** Un group, **(f)** Gxy group, and **(g)** Gz group. **(h)** FEA model after assembly

Table 1 The material parameters used in the FEA

Material	Elastic modulus(MPa)	Poisson ratio
Implants	103,400	0.35
Cortical bone	13,700	0.3
Cancellous bone	5500	0.3

Table 2 The 3D printing parameters

Powder thickness	Laser power	Scar speed	Energy density	Atmosphere
(μm)	(W)	(mm/s)	(J/mm^3)	
15–53	190 W	300	254.41	Argon

The porous scaffolds were gold-coated for 45 s, and their morphology was subsequently imaged using a Hitachi Regulus 8100 scanning electron microscope (Hitachi High-Technologies Corporation Japan). The imaging was conducted at an accelerating voltage of 3 kV.

Mechanical compression test of porous scaffolds

To evaluate the mechanical properties of the porous Ti samples, compression testing was performed using an Instron 3369 tester (Instron, USA) in displacement control mode with a cylindrical sample (20 mm in height and 10 mm in diameter). A vertical force was applied to the scaffold at a rate of 0.5 mm/min under computer-controlled conditions until fracture occurred (Fig. 3a, b).

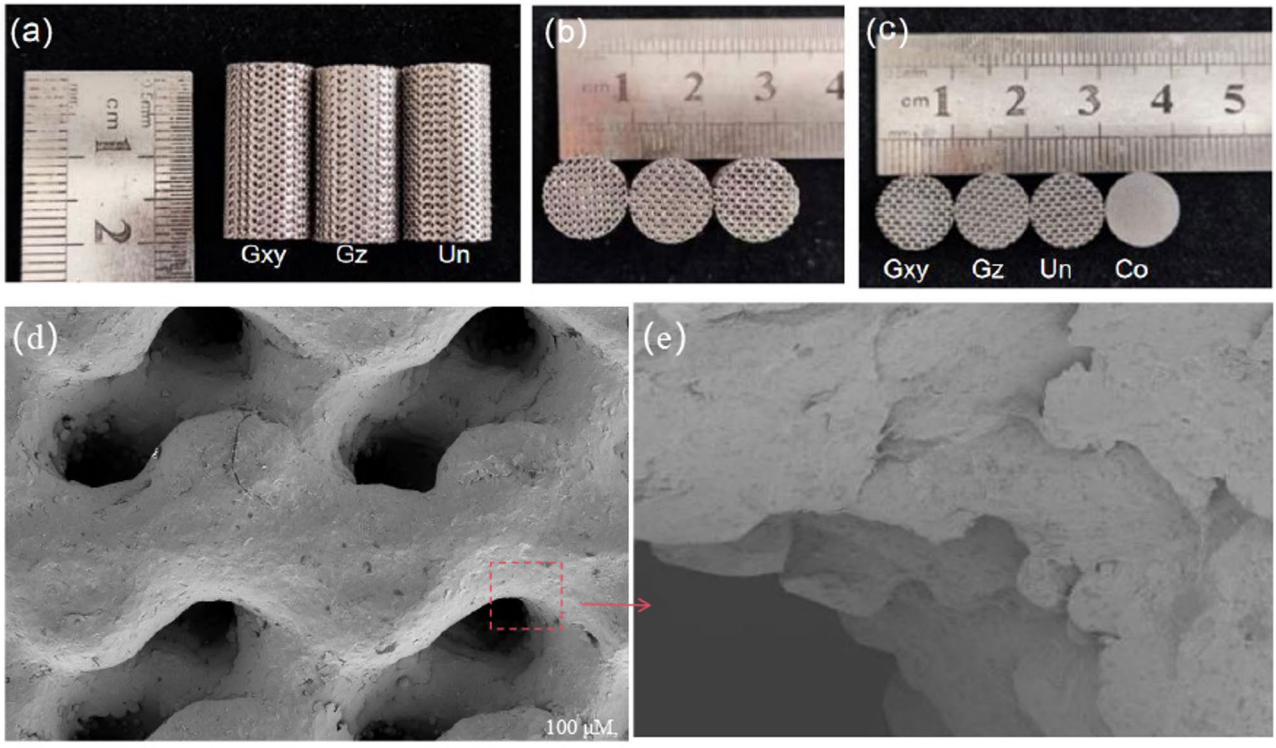

Fig. 2 Cylindrical porous scaffolds used for mechanical testing. **(a)** Lateral views and **(b)** top views of three experimental groups. **(c)** Disc-shaped scaffold used for cell experiments. Scanning electron microscopy (SEM) images of porous scaffolds. **(d)** The red dashed box indicating the high-magnification area and **(e)** enlarged view of the porous structure

A stress-strain curve was generated from the static compression test results for each scaffold.

In vitro biological properties of porous scaffolds

Rat bone mesenchymal stem cells (rBMMSCs) (Shanghai Fuheng Biotechnology Co., China) were cultured and passaged. Passages 3 to 5 of rBMMSCs were used in this study. The porous scaffolds for cell culture assays were designed as discs with a diameter of 10 mm and a thickness of 3 mm. A dense titanium disc of the same size served as the control (CO) for the in vitro cell test (Fig. 2c). Sterile porous scaffolds were arranged and placed in 24-well plates. Cells were counted, diluted to the appropriate density, and seeded onto the scaffolds. For cytotoxicity and proliferation experiments, the inoculum size was 5 × 10^4 cells/well, with 1 mL of medium per well. For the osteogenic differentiation experiment, 2 × 10^4 cells/well were seeded with 1.5 mL of medium per well.

Live/dead staining was performed to assess the effects of different porous scaffolds on the activity of rBMMSCs. A total of 300 μL of staining solution was added to each well containing the scaffold, and the cells were incubated at 37 °C for 30 min under light protection. The wells were then washed twice with PBS (Wuhan Saiwell Biotechnology Co., LTD., China). After incubation, the mixture was observed using an inverted fluorescence microscope (ZEISS, Germany). rBMMSCs were seeded into scaffolds. After 1, 4, and 7 days, the medium was carefully removed from each well, and the wells were washed with phosphate-buffered saline (PBS). Then, 1 mL of Cell Counting Kit-8 (CCK-8) solution (Biyuntian Biotechnology Co., LTD., China) was added to each well, and the cells were incubated at 37 °C in the dark for 2 h. After incubation, 100 μL of the supernatant from each well was transferred to a 96-well plate. The absorbance (OD) at 450 nm was measured using a microplate reader to evaluate the proliferative behavior of rBMMSCs on the porous scaffolds.

Following the inoculation procedure, the culture medium was replaced with osteogenic medium. High-glucose medium and fetal bovine serum (both from Biological Industries, Israel) were mixed at a 10:1 ratio to prepare a 50 mL pre-mixture. To this medium, 2 mL of β-glycerophosphate disodium salt working solution (Aladdin Biochemical Technology Co., Ltd., China), 50 μL of ascorbic acid working solution (Aladdin Biochemical Technology Co., Ltd., China), and 10 μL of dexamethasone working solution (Sigma Company, USA) were added. The detailed preparation of the medium was described in previous studies [28] and alkaline phosphatase (ALP) staining was performed using a BCIP/NBT kit (Biyuntian Biotechnology Co., LTD., China). Images

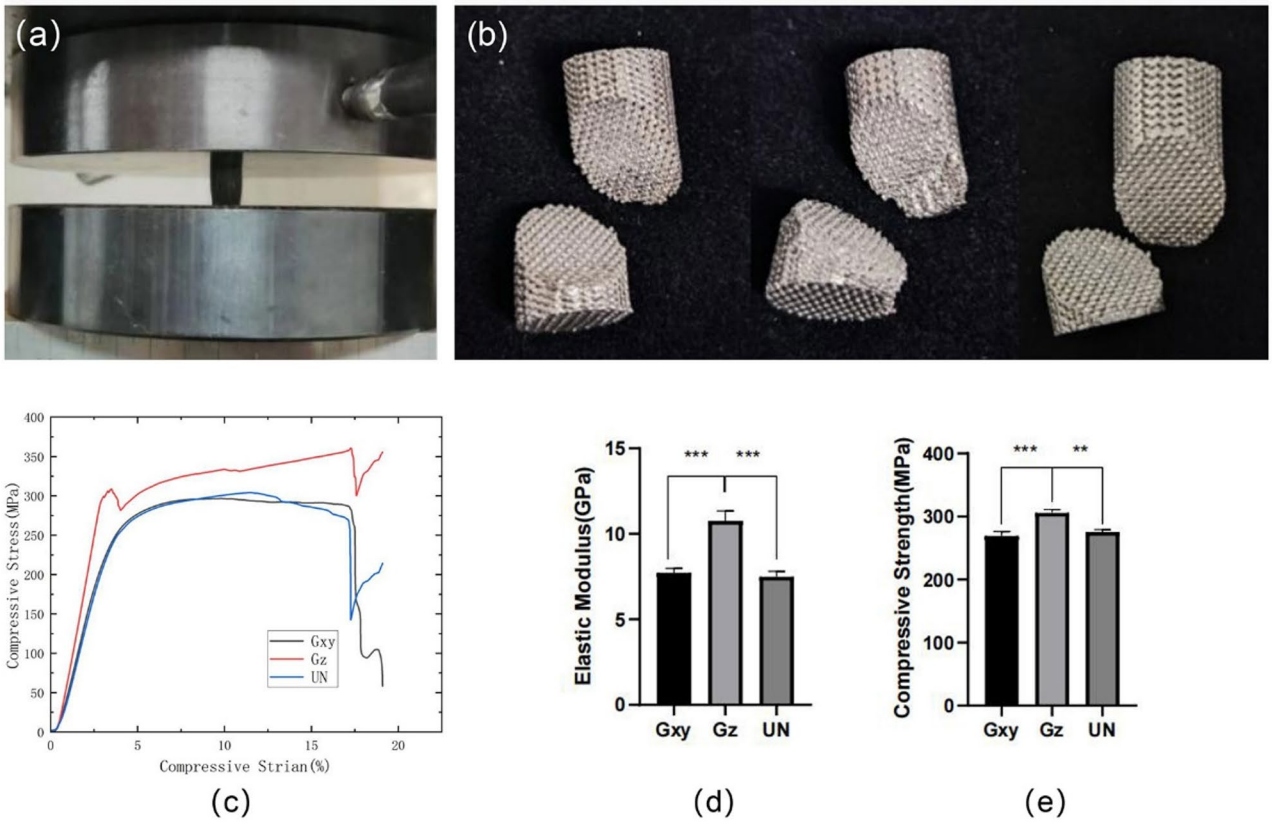

Fig. 3 Mechanical compression experiment of porous scaffolds. **(a)** Compression process and **(b)** fracture cross-sections of the 3 experimental groups. **(c)** Stress-strain curves obtained from compression tests. **(d)** Elastic modulus of different scaffold groups. **(e)** Compressive strength of different scaffold groups

were taken, and the scaffolds were recorded after they were dried. Additionally, the scaffolds and the concentration of seeded cells were stained with ALP. The staining protocol remained the same, and osteogenic induction was extended to 14 days, with determinations made on days 7 and 14. Following the kit's instructions, 50 μL of detection reagent was added to each well and incubated at 37 °C in the dark for 30 min. The OD value at 405 nm was measured using a microplate reader, and the standard curve was used to calculate the ALP activity.

Preparation of PDGF-BB/BMP-2 chitosan microsphere coating and composite scaffolds

Lyophilized BMP-2 (China Pharmaceutical and Chemical Import and Export Co., Ltd.) and PDGF-BB powders (China Pharmaceutical and Chemical Import and Export Co., Ltd.) were centrifuged at high speed to collect proteins adhered to the cap or walls of the tubes. The powders were then dissolved in sterile deionized water reconstitution buffer (China Pharmaceutical and Chemical Import and Export Co., Ltd.), resulting in the complete solubilization of the BMP-2 and PDGF-BB to obtain solutions with concentrations not less than 100 μg/mL. An appropriate amount of chitosan powder (McLean Biochemical Technology Co., Ltd., China) was combined with 1% acetic acid solution (Tianjin Damao Chemical Reagent Factory, China) and shaken until a homogeneous, viscous chitosan solution was obtained. The pH was adjusted to 5 using saturated sodium hydroxide solution(Shanghai Maclean's Biochemical Technology Co. Ltd., China), after which sodium tripolyphosphate (TPP) solution (McLean Biochemical Technology Co., Ltd., Shanghai, China) was added at a concentration of 0.8 mg/mL, maintaining a mass ratio of chitosan to TPP of 3:1. The suspension was prepared by magnetic stirring at room temperature for 1 h. The BMP-2 and PDGF-BB solutions were added slowly to the suspension and stirred for 30 min, resulting in a milky white solution. Three chitosan microsphere solutions containing different growth factors were obtained (Fig. 4a). Next, 2.5 mL of chitosan microsphere solution enriched with different growth factors was added to the sterilized porous scaffolds and frozen. The scaffolds were then transferred to a vacuum freeze dryer (Shanghai Shenyang Instrument Co., Ltd., China) for freeze-drying, resulting in scaffolds in the form of a white powder (Fig. 4b, c). All coating procedures were conducted under sterile conditions inside a biosafety cabinet (Shanghai Senxin Experimental

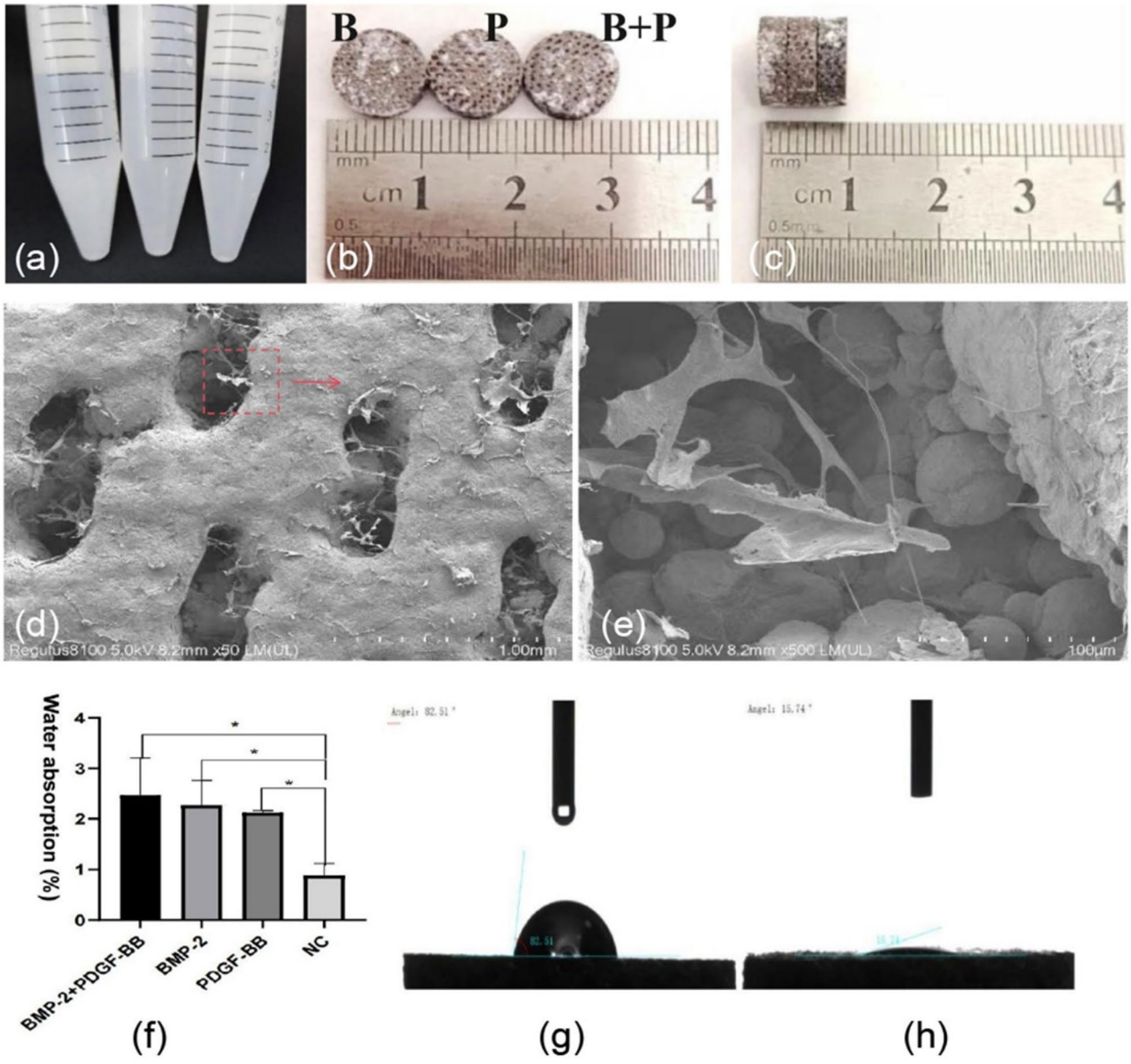

Fig. 4 **(a)**PDGF-BB Chitosan microsphere solution, BMP-2 Chitosan microsphere solution, and PDGF-BB /BMP-2 combined Chitosan microsphere solution. **(b)** Top and **(c)** lateral views of three types of composite scaffolds. SEM images of composite scaffolds. **(d)**. The red dashed box indicates the high magnification area and **(e)** Detailed visualization of chitosan microsphere distribution within the scaffold. White mesh structure is chitosan microsphere. **(f)** Water absorption test results comparing different composite scaffolds and uncoated scaffolds. Wettability test results of composite stents and uncoated scaffolds. **(g)**. Uncoated scaffold group and **(h)** Coating scaffolds Group

Instrument Co.) to ensure contamination-free handling. Detailed Preparation Steps of Chitosan Microspheres Containing Different Growth Factors are provided in Supplementary File 1. Three different sets of composite scaffolds were obtained: porous scaffolds modified with chitosan microspheres carrying BMP-2 (B group), PDGF-BB (P group), or both BMP-2 and PDGF-BB (B + P group). Additionally, uncoated porous scaffolds were used as a control group (NC group).

Characterization of the composite scaffold

The particle size of chitosan microspheres on the surface of the composite scaffold was observed by the same SEM equipment under identical conditions.

An equilibrium swelling test was used to detect the water absorption of composite scaffolds. The calculation formula is as follows:

$$(E_{sw}\,(\%) = \frac{W_e - W_0}{W_0} \times\ 100) \tag{2}$$

W_e: weight of solution after immersion. W_0: weight of bracket before immersion.

The wettability of the composite scaffold was tested by the seat drop method. The sample was placed on the contact Angle test platform, and water drops were slowly injected from the top of the sample through the automatic titration system of the JY-82 C contact Angle measuring instrument (Chengde Dingsheng Testing Machine Testing Equipment Co., LTD., China), and the test photos were taken. Finally, the picture of the initial contact between the droplet and the sample was selected, the contact Angle was taken for the high dosage method, and the measurement range was $0° < \theta < 180°$.

In vitro experiments of PDGF-BB/BMP-2 chitosan microsphere-coated composite scaffolds

The composite scaffolds were co-cultured with rBMMSCs for 1, 3, and 7 days, and 1 mL of prepared CCK-8 solution (Beyotime Biotechnology Ltd.) was added to each well at the corresponding time points. The OD was measured using an Epoch enzyme-labeled instrument (Thermo Fisher Company, USA).

For osteogenic induction, the cells were co-cultured with composite scaffolds in a 5% CO2 incubator at 37 °C for 24 h, and the original medium was replaced with an osteogenic induction medium every 3 days. On days 0, 5, 7, 14, and 21 of culture, the cells were rinsed twice with PBS (Wuhan Sevier Biotechnology Co., Ltd., China), fixed with 4% paraformaldehyde for 30 min, and then washed again with PBS for subsequent osteogenic induction experiments. On the 7th day of osteogenic induction culture, the cells on the composite scaffold were stained using a BCIP/NBT kit (Biyun Tianshi Technology Co., China). An appropriate amount of pre-staining working solution was added to each well, ensuring that the composite scaffolds were submerged. The staining solution was discarded at the end of the incubation at room temperature and protected from light. The cells were washed gently with PBS twice, air-dried, and then observed and photographed.

The ALP activity of cells cultured on the composite scaffolds was assessed using an alkaline phosphatase assay kit on days 7 and 14 of osteogenic induction.Each well was treated with 200 μL of RIPA cell lysate (Beijing Solaibao Technology Co., Ltd., China), followed by centrifugation at 12,000 rpm and 4 °C for 20 min. Standard wells, blank control wells, and sample wells were prepared. All wells, except the standard wells, were supplemented with 50 μL of color development substrate, and absorbance values were measured using a microplate reader. A standard curve was generated based on the OD values obtained from the standard and blank control wells. On day 21 of osteogenic differentiation, 1 mL of 2% alizarin red S staining solution (Beijing Solepol Science and Technology Ltd., China) was added to each well and incubated at room temperature for 30 min before observation and imaging. After staining, the 24-well plate was air-dried in a ventilated area. To quantify mineralization, 1 mL of 10% CPC solution (Aladdin Biochemical Technology Co., Ltd., China) was added to each well to dissolve the mineralized nodules. Subsequently, 200 μL of the dissolved solution was transferred to a 96-well plate, and the OD value was measured at the specified wavelength using a microplate reader.

In vivo experiments of PDGF-BB/BMP-2 chitosan microsphere-coated composite scaffolds

All male Sprague-Dawley (SD) Rat used in this experiment were obtained from Zhejiang Viton Lihua Laboratory Animal Technology Co. All SD rats were housed in an environment of 20–30 °C (temperature) and about 50% (humidity). At the beginning of the experiment, all rats were 10 weeks old and weighed 350 g ± 20 g.

Systemic toxicity analysis of composite scaffolds

Composite scaffolds were implanted into SD rats in groups. The heart, liver, spleen, lungs, kidneys, and other major organs of the SD rats were put into a 4% paraformaldehyde solution, and the tissues were cut for HE staining, sealed, and then observed under the microscope and recorded.

Implantation operating procedures and micro-CT analysis

12 SD rats were randomly divided into 4 groups of 3 rats each. B group, P group, B + P group, Blank control group (no stent material implanted for repair). Each rat was grouped and labeled, the rats were anesthetized intraperitoneally with 1% sodium pentobarbital solution, the hair was removed, the operation area was disinfected, and the bone was drilled with a sterile annular coring tool (Shanghai McLean Biochemical Technology Co., China) to form a bone defect with a diameter of 3 mm and a depth of 4 mm at the location of the lateral femur slide on both sides (Fig. 9b), and the composite scaffolds was implanted into the hole (Fig. 9c)and no implantation in the blank control group. Local intramuscular injection of cefazolin sodium solution (Shanghai McLean Biochemical Technology Co., China) was given once a day for 1 week to prevent infection after the operation.

The rats were killed by intraperitoneal injection of 1% pentobarbital sodium solution at 4-, 8-, and 12 weeks post-implantation, and the bone tissue around the composite scaffolds were retrieved (Fig. 9d, e). The bone specimens were scanned using a Micro-CT/in vivo imaging system (MILabs B.V., Netherlands), and three-dimensional reconstruction of the bone tissues surrounding the composite scaffold and within the foramen was performed using MILabs Rec software (Hunan Huashu

High-Tech Co., China). Subsequently, Imalytics Preclinical 3.0 software was employed to analyze the parameters of newly formed bone in the reconstructed region, including bone volume (BV) and total volume (TV). The bone volume fraction (BV/TV) was then calculated to quantitatively assess the bone regeneration capacity of each group, with a higher ratio indicating superior osteogenic potential. In the experimental group, the TV was defined as the volume of the implanted scaffold multiplied by its total porosity, whereas in the blank group (without scaffold implantation), the TV corresponded to the total volume of the bone defect at the time of modeling (diameter: 3 mm; height: 4 mm).

Hard tissue embedding, sectioning, and Van Gieson (VG) staining

Hard tissue sections of the above specimens were stained at weeks 4 and 12 after surgery: Determine the sampling site, use a diamond osteotome (Eckat Ltd., Germany) to cut, then 4% paraformaldehyde(shanghai Maclin Biochemical Technology Co., Ltd) fixation of bone tissue, 70% formaldehyde-acetic acid–alcohol (Wuhan Sevier Biotechnology Co., China)fixation of plant tissue, and put into graded alcohol dehydration. After dehydration, the samples were infiltrated with T7200 resin (Wuhan Sevier Biotechnology Co., China) and embedded. The hard tissues were ground, rinsed with Weight iron hematoxylin stain (Wuhan Sevier Biotechnology Co., LTD), and finally stained with an acidic magenta solution (Wuhan Sevier Biotechnology Co., LTD). The slices were observed under the microscope.

Statistical analysis

All experiments were repeated at least three times, and representative graphs are shown. The data are expressed as mean ± SD. Statistical analysis was performed using GraphPad Prism 8.3.0. One-way ANOVA followed by Tukey's post hoc test was used for multiple group comparisons. P value < 0.05 was considered statistically significant.

Statistical significance is indicated as * $P<0.05$, ** $P<0.01$, *** $P<0.001$, **** $P<0.0001$.

Results

Characterization of porous scaffolds and composite scaffolds

The SEM images of the 3D-printed porous scaffold (Fig. 2d, e) showed that the pore structure of the porous scaffolds was relatively homogeneous, with good connectivity and no fracture, and no obvious unmelted particles were seen. The surface of the composite scaffold (Fig. 4d, e) was covered with a reticular structure, and the inner surface was covered by chitosan microspheres.

By measuring the actual diameter and height of the porous scaffolds and weighing each group of porous stents on a precision electronic balance, the average porosity was calculated to be 47.75% for the Gxy group, 49.97% for the Gz group and 49.25% for the UN group. The measured porosities were slightly lower than the designed porosities, but the difference was small. Porosity, pillar radius, and pore size were comparable to the design model, indicating high print quality in this study.

The results of the water absorption rate test of the porous scaffolds (Fig. 4f) showed that the water absorption rate of the experimental group is better than that of the control group, the difference is statistically significant, and the difference between the experimental groups is not statistically significant. The wettability test of the stent is shown in Fig. 4g and h. The water droplets of the uncoated group cannot quickly disappear into the stent, which is standing on the surface of the stent with a large contact angle; the water droplets of the composite stent group can quickly penetrate the stent with a small contact angle. It indicates that the chitosan-coated scaffolds have better wettability than uncoated scaffolds and can improve the hydrophilicity of the scaffold surface.

Mechanical properties of porous scaffolds

The equivalent stresses of gradient porous implants were smaller than those of the non-gradient porous group under both axial and oblique loading. The maximum equivalent stress in the cortical bone of the gradient porous implant group was greater than that of the solid and uniform porous groups (Fig. 5), which indicated that more stress was transmitted to the peri-implant area when external forces were applied, reducing the "stress shielding" phenomenon. On the other hand, under the same uniform porosity, the stress distribution of the uniform and radial gradient scaffolds was similar and more uniform than that of the axial gradient scaffolds. The maximum equivalent force for all groups of implants was not very different, which could be since the periphery of the implant is composed of dense structures.

Figure 3c shows the stress-strain curves of the porous scaffolds in three groups. The elastic modulus was calculated from the slope of the original straight-line deformation zone on the curves: the average was 7.72 ± 0.26 GPa for the Gxy group, 10.75 ± 0.59 GPa for the Gz group, and 7.50 ± 0.31 GPa for the UN group. The compressive strength of the porous titanium alloy scaffolds was 269.23 ± 6.91 MPa in the Gxy group, 305.86 ± 5.41 MPa in the Gz group, and 275.65 ± 3.46 MPa in the UN group, and the compression tests showed that the differences in the modulus of elasticity and compressive strength of the Gxy group and the UN group were smaller and the modulus of elasticity. Among the three groups, the modulus of elasticity and compressive strength of the Gz group

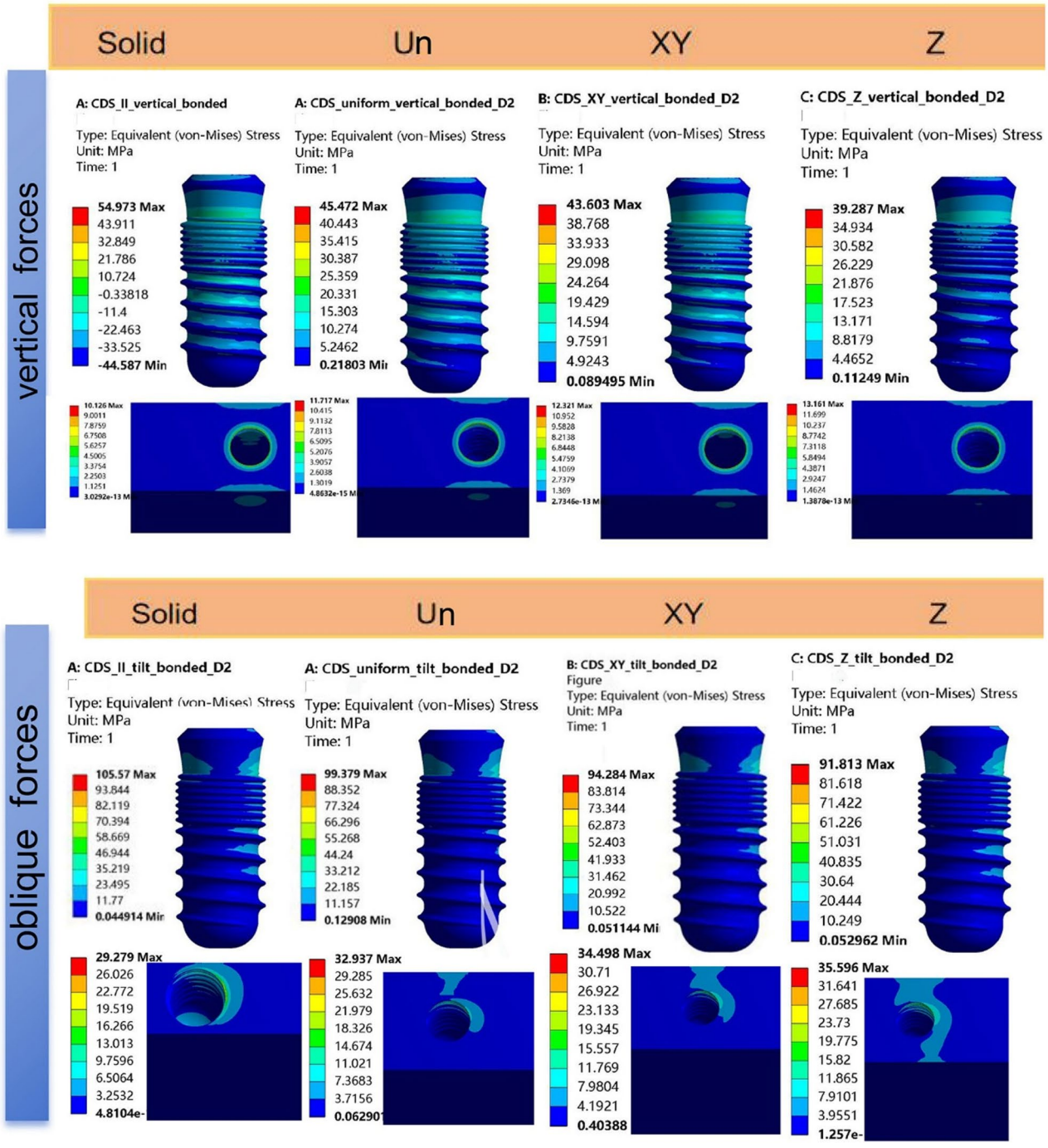

Fig. 5 Von Mises stress contours of different implants and cortical bone when different implants were under oblique or vertical loading conditions

were higher than those of the other two groups (Fig. 3d, e). The Gz group has the highest compressive strength (305 MPa), which is approximately 1.5 times higher than that of human cortical bone (180.5-211.1 MPa), indicating better mechanical properties. The modulus of elasticity of three groups of porous titanium alloys was within the range of the modulus of elasticity of natural human bone (0.05-30 GPa) [29].

Cytocompatibility and osteogenesis property of porous scaffolds

Immunofluorescence electron micrographs of cells co-cultured with three types of porous and dense scaffolds and rBMMSCs at 1, 4, and 7 days are presented in Fig. 6. The rBMMSCs exhibited favorable morphology and adhered well to the scaffold surfaces across all groups, with no significant morphological differences observed

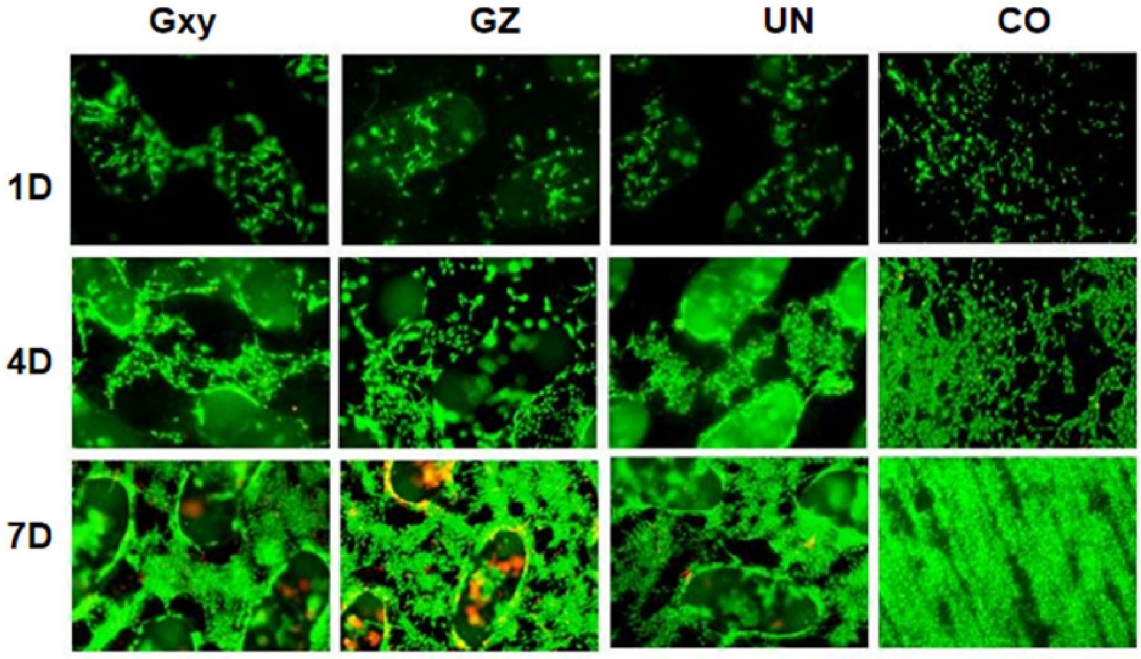

Fig. 6 Immunofluorescence electron micrographs of rBMMSCs cultured on scaffolds. Live cells are stained green, while dead cells are stained red

between groups. By day 4, a substantial increase in cell number was evident on all scaffolds compared to day 1. This proliferation continued through day 7, with cells covering nearly the entire scaffold surface in all groups and only minimal cell death observed. These findings demonstrate that all four scaffolds possessed excellent in vitro cytocompatibility.

As shown in Fig. 7a, the OD values progressively increased across all groups with longer co-culture durations, indicating a positive correlation between rBMMSC proliferation and culture time - a finding consistent with the Live/Dead staining results. On day 1, the CO group exhibited the highest OD value; however, its growth rate became progressively slower than other groups over time. This phenomenon may be attributed to the solid disc's extensive initial cell contact area, which promoted adhesion but limited subsequent proliferation space. The Gxy group demonstrated the highest OD values on days 4 and 7, suggesting the most pronounced rBMMSC proliferation on these scaffolds. No statistically significant differences were observed between the Gz, UN, and CO groups by day 7.

ALP serves as a hallmark enzyme during the differentiation of BMMSCs into osteoblasts. To verify osteogenic differentiation, rBMMSCs were analyzed through ALP staining [30], with results presented in Fig. 7b. As an early marker of osteogenic differentiation, ALP activity levels effectively demonstrate the influence of various porous scaffolds on rBMMSC osteoinduction. During the 7- and 14-day induction period, the Gxy group exhibited the highest ALP activity, followed by the Gz and UN groups, with no statistically significant difference observed between the latter two groups. Notably, all three porous scaffold groups demonstrated significantly greater ALP activity compared to the CO group (Fig. 7c), suggesting that rBMMSCs cultured on Gxy group scaffolds possess enhanced osteogenic differentiation potential.

Cytocompatibility and osteogenesis property of PDGF-BB/BMP-2 chitosan microsphere-coated composite scaffolds

Through preliminary experiments, radial-gradient porous scaffolds (Gxy) were selected to be composite with different growth factors to obtain different composite scaffolds(B group, P group, B + P group), and selected uncoated radial gradient porous scaffolds as controls (NC group).

In vitro experiments

The proliferation of rBMMSCs on various coated composite scaffolds was evaluated using CCK-8 assays after 1, 3, and 7 days of co-culture. As shown in Fig. 8a, optical density (OD) values increased progressively across all groups with extended culture duration. While no significant differences in cell proliferation were observed among groups on day 1, the experimental groups demonstrated significantly higher absorbance values compared to the control group at days 3 and 7 ($p < 0.05$), confirming the non-cytotoxic nature and proliferative enhancement of the composite scaffolds. Notably, the B + P group exhibited the highest cell density, suggesting synergistic

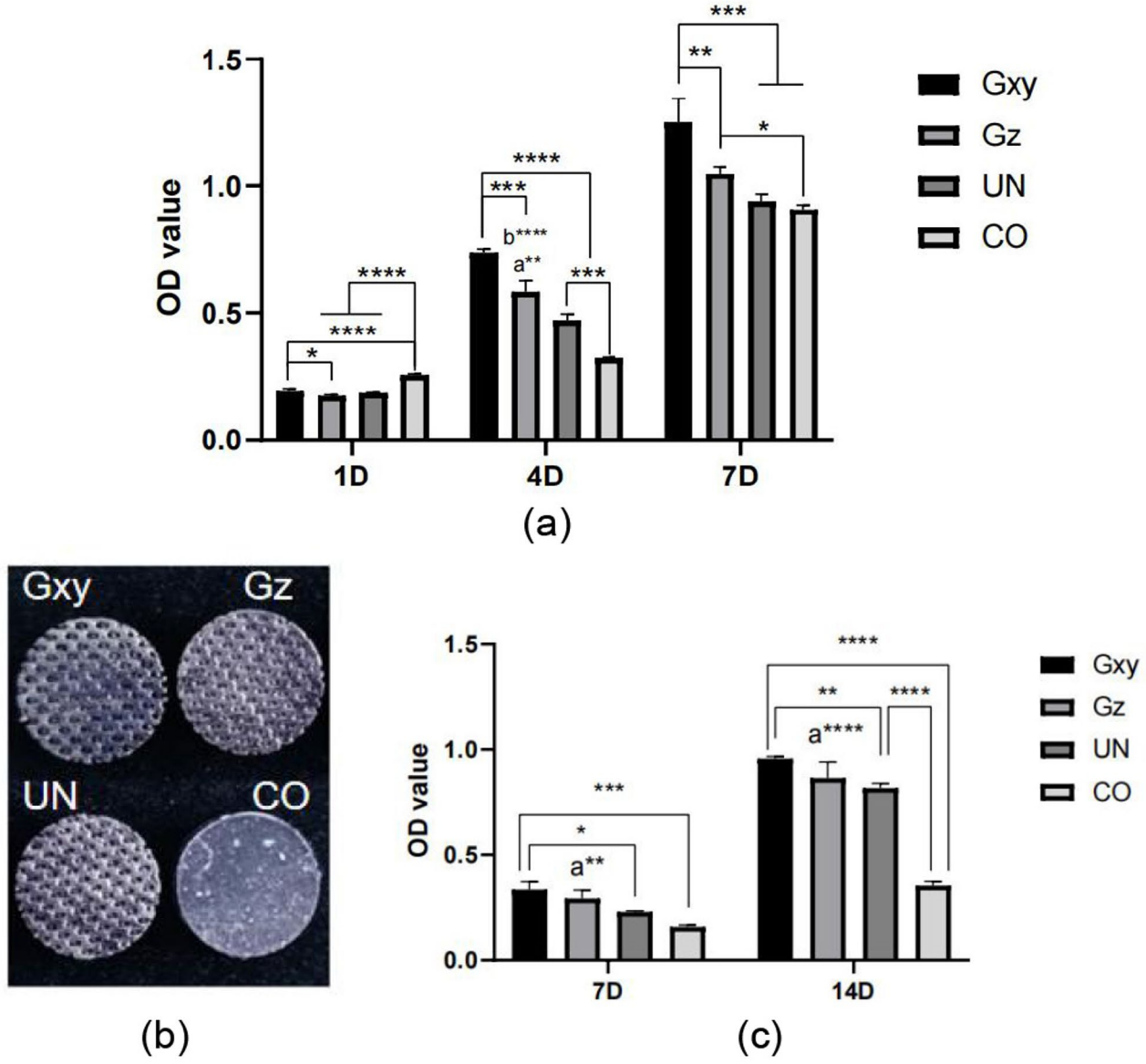

Fig. 7 **(a)** Proliferation of rBMMSCs on scaffolds in different groups, assessed at designated time points. Statistical comparisons: a: vs. UN group, *b*: vs. CO group. **(b)** ALP staining of scaffolds. Where ALP-positive cells appear blue, while undifferentiated cells remain unstained. **(c)** Quantitative analysis of ALP activity after 7 and 14 days of osteogenic induction. a: Vs CO group

effects of bifactor coating superior to monofactor applications.

The results of ALP staining after 7 days of differentiation are presented in Fig. 8b. Throughout the 7- and 14-day differentiation periods, the highest alkaline phosphatase activity was observed in the B + P group, with all experimental groups displaying significantly greater ALP activity than the control group (Fig. 8d). These findings indicate that although scaffolds coated with either B or P alone exhibited enhanced osteogenic potential, the combined B + P treatment yielded superior osteogenic differentiation outcomes.

Alizarin red staining demonstrated calcium nodule formation, a characteristic feature of late-stage osteogenesis in rBMMSCs. After 21-day differentiation, the B + P group showed maximal mineralization (Figs. 8c, e), with all experimental groups exceeding the control ($p < 0.05$), though B + P and B groups showed comparable results ($p > 0.05$).

In vivo experiments

All rats recovered well from anesthesia and the operative procedure. No implant dislocation or incision infection occurred during the experiment. HE staining microscopic observation results (Fig. 9a) indicated that no

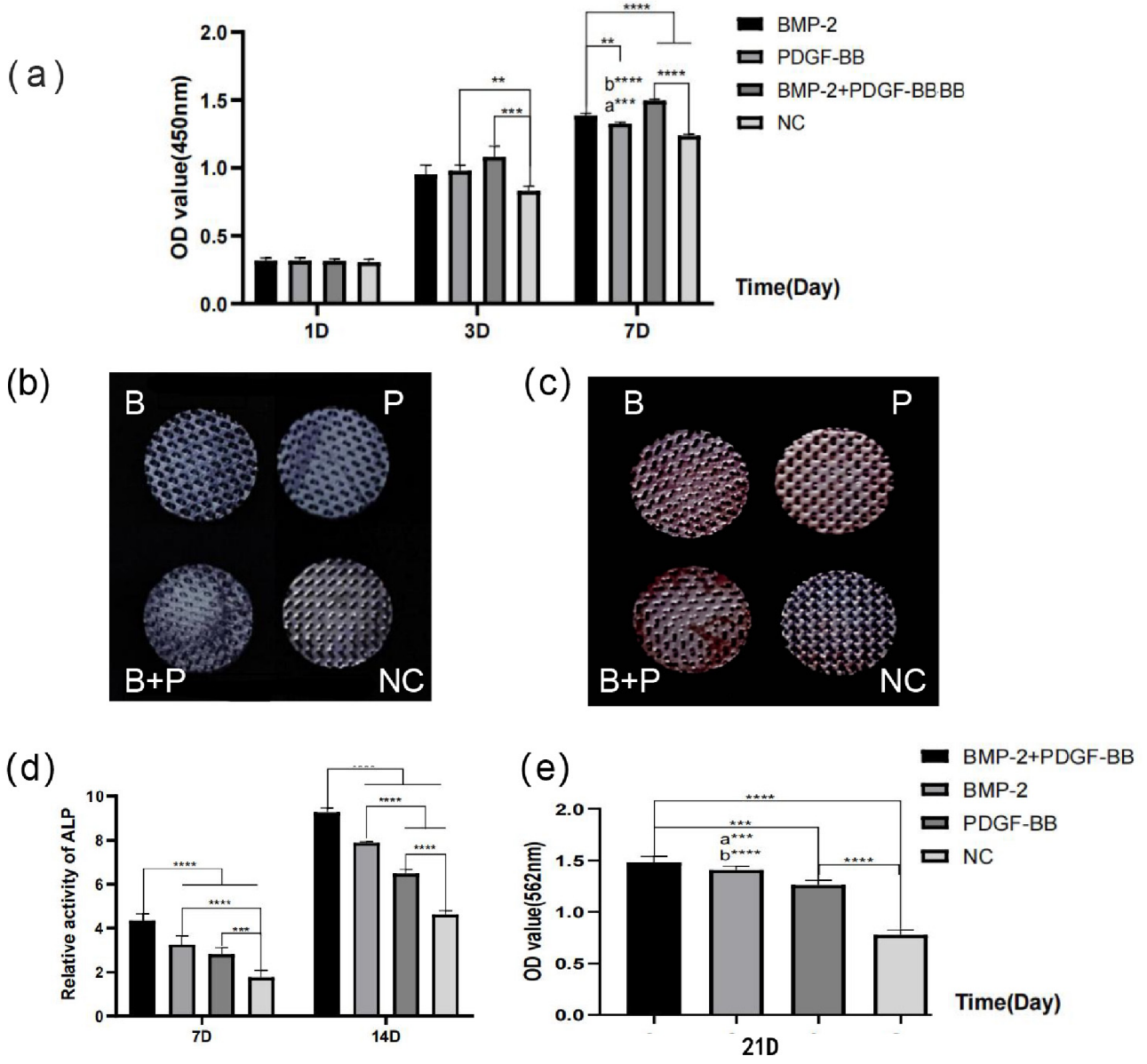

Fig. 8 **(a)** Proliferation ability of rBMMSCs cultured on different composite scaffolds, analyzed at specified time points. a: vsNC group, b: vsBMP-2 + PDGF-BB group. **(b)** ALP staining of composite scaffolds after 7days of co-culturing. **(c)**. Alizarin Red Staining of composite scaffolds after 21 days of co-culture **(d)**. ALP activity quantification of different coated scaffolds at 7 and 14 days. (**e**) Semi-quantitative analysis of mineralized matrix deposition in composite scaffolds after 21 days of co-culture

pathological lesions were observed in the microscopic structures of the organs across all groups at each observation time, suggesting that the composite structural material exhibited no apparent toxicity to rats and demonstrated good biological safety.

Micro-CT observation results (Fig. 9f) revealed that new bone growth was observed on the surfaces and within the pores of the porous titanium alloy scaffolds across all experimental groups and time periods, suggesting that all three scaffold composites exhibited superior bone-repairing capabilities.

The ability of each scaffold composite group to promote new bone formation was further evaluated by calculating the bone volume fraction (BV/TV), and the changes in new bone volume across groups were analyzed over time. As shown in Fig. 10a, b and c, the bone volume fractions in all titanium alloy scaffold implantation groups were significantly higher than those in the blank control group ($p < 0.001$). Notably, the B + P group exhibited greater new bone formation than the B-alone and P-alone groups. Notably, the B + P group exhibited greater new bone formation than the B-alone and P-alone groups ($p < 0.001$). At 4 weeks, the B group demonstrated

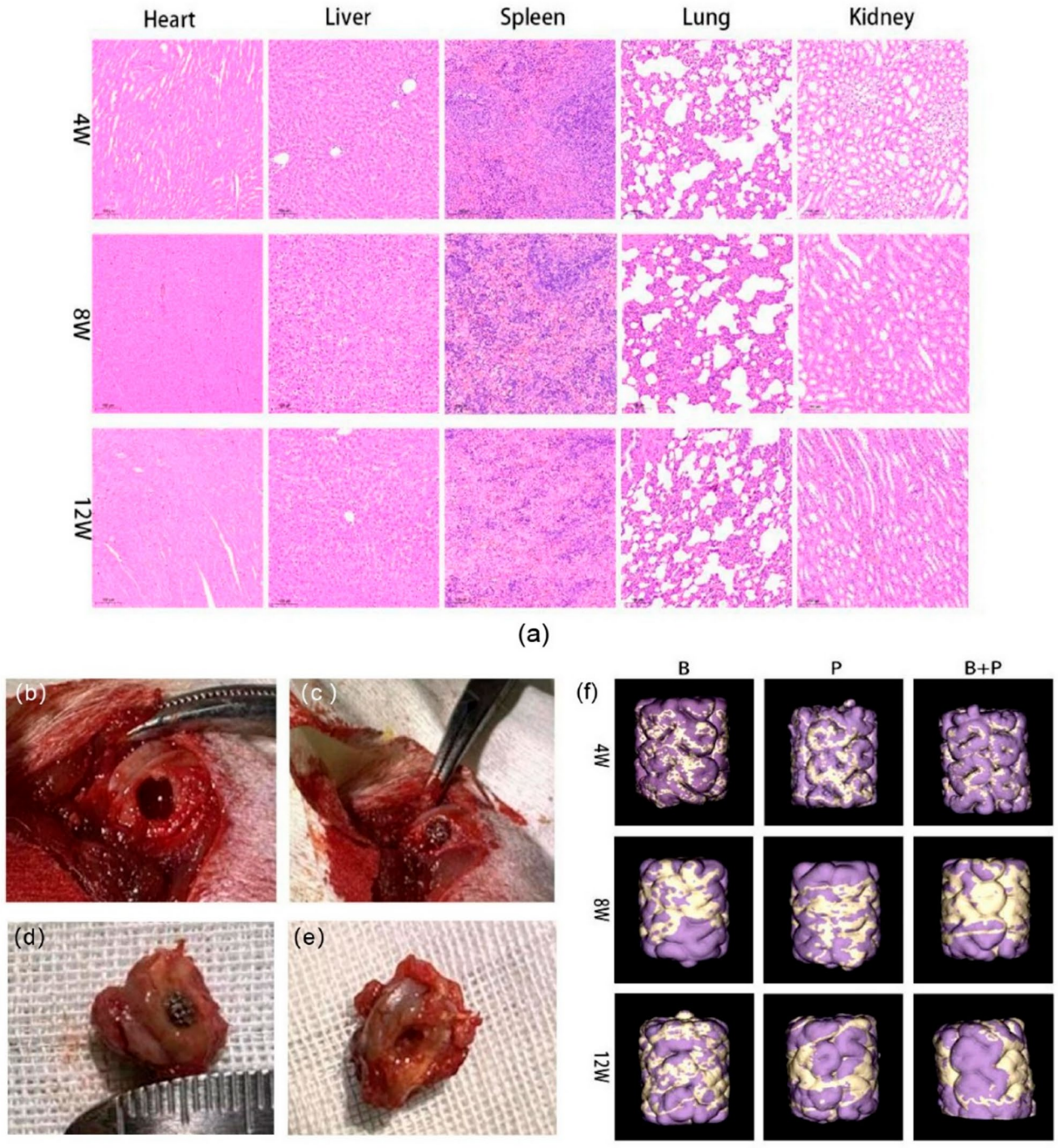

Fig. 9 Histological and radiographic evaluation of scaffold implantation in vivo. **(a)** HE staining results of major organs from SD rats. **(b)** Surgical procedure for establishing bone defect models. (**c**) Subperiosteal implantation of scaffolds at the defect site. **(d)** Retrieved bone specimen from the blank control group, showing an unused scaffold. **(e)** Retrieved bone specimen from the experimental group, demonstrating composite scaffold integration. **(f)** Micro-CT reconstruction results: the purple region represents the scaffold, while the yellow region represents newly formed bone tissue

significantly higher new bone formation than the P group ($p < 0.05$); however, no statistically significant difference was observed between these groups at 8 and 12 weeks ($p > 0.05$). Furthermore, the new bone volume increased with healing time in all groups, with significantly greater bone formation at 12 weeks compared to 4 and 8 weeks ($p < 0.001$), as illustrated in Fig. 10d.

The osseointegration of titanium scaffold composite structures in each group was assessed using Van Gieson (VG) staining. As illustrated in Fig. 11, new bone

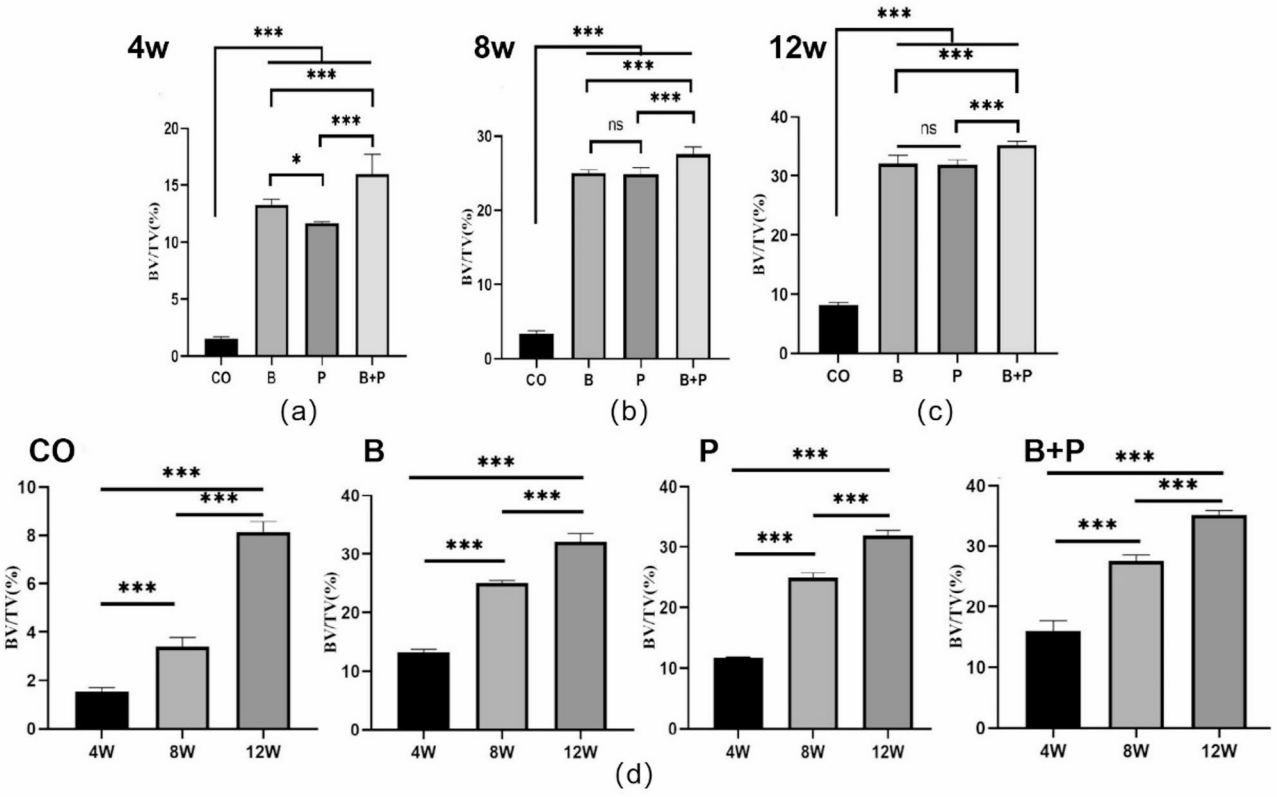

Fig. 10 Analysis of BV/TV values between groups at different observation periods: (**a**) 4 weeks, (**b**) 8 weeks, and (**c**) 12 weeks. ns: $p > 0.05$, not statistically significant. **(d)** Comparison of BV/TV values overtime within each group

formation was observed at the surface boundaries of the porous scaffolds in all groups by the 4th week post-implantation, with no evidence of inflammatory cell infiltration or foreign body reaction, indicating favorable osseointegration. By the 12th week, new bone tissue had also formed within the central regions of the scaffolds. Notably, the B + P group exhibited superior new bone formation compared to the B-alone and P-alone groups, which was consistent with the micro-CT findings.

Discussion

Osseointegration is a prerequisite for predicting implant success, and biocompatible surface structure and properties of implants are an important part of the factors that influence osseointegration [31]. Therefore, improving implant design to achieve higher osseointegration rates and strength for longer service life is the focus of current research. The microstructure of the implant surface is closely related to the achievement of good osseointegration.3D printing technology can produce implants with precise surface microstructure due to its sophisticated manufacturing process.

This study systematically compared the mechanical properties and biocompatibility.

of porous structures with different gradient orientations. The SEM images clearly show the uniformity of the pore structures and their interconnectivity across all scaffold groups. The interconnected pores are essential for nutrient and waste diffusion and would be beneficial for body fluids circulation, nutrient and oxygen transport, vascularization, and bone ingrowth [32]. The roughness observed in the SEM images suggests that the surface of the porous support has a certain degree of roughness. Previous studies have shown that surface roughness enhances the adsorption of proteins and growth factors, which are essential for cell proliferation and differentiation [33].

According to the finite element analysis and compression test in this study, the porous implants had a stronger stress transfer capacity compared to solid structures, and the stress distribution of the uniform and radial gradient scaffolds was similar. Research indicates that scaffolds with radial gradient porosity result in more uniform stress distribution. This design reduces the stiffness of titanium alloys and alleviates stress shielding effects [34]. In gradient scaffolds, stress concentration occurred at both ends, with stress conduction affected by pore size variations. The stress applied on axial struts decreased from top to bottom, while radial struts maintained

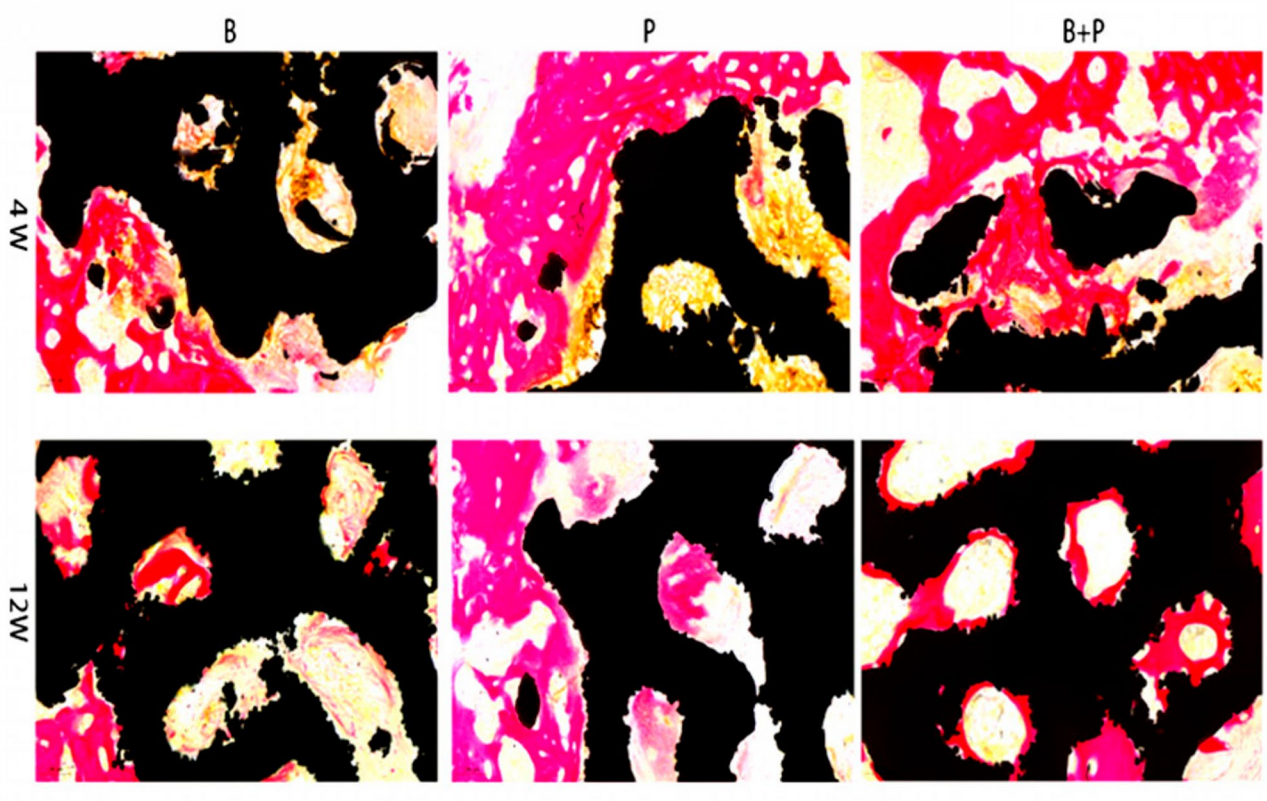

Fig. 11 VG staining of hard tissue sections. Black regions represent composite scaffolds, while red areas indicate newly formed bone tissue

low-stress levels [35]. The compressive strength and peak stresses of Gz were significantly higher than those of the Gxy and Un groups. This phenomenon may be attributed to the gradient variation along the Z-axis, where porosity gradually increases from top to bottom. Such an arrangement mimics the elastic modulus of alveolar bone, with the low porosity at the top resulting in an elastic modulus comparable to that of cortical bone, while the high porosity at the bottom enables the porous structure to exhibit an elastic modulus similar to that of cancellous bone. one ingrowth during the healing process. The natural bone has a graded structure, the outer cortical bone is solid and dense, and the inner cancellous bone is a spongy honeycombed structure [36]. The elastic modulus of all three groups was close to the elastic modulus of cancellous and cortical bone (0.5–20 GPa). For implants, it is of great significance to possess the appropriate biomechanical properties to adapt to natural bones [37]. excessive mechanical properties will lead to stress shielding [38], while too small mechanical properties cannot maintain the space maintenance of scaffolds, resulting in bone resorption [39]. Moreover, biomechanical properties also influence cell behaviors and modulate the local environment [40]. Our results suggest that all three porous structures can meet the implant placement strength within the appropriate range of porosity and pore size.

Next, the biocompatibility of porous scaffolds was observed. Cytocompatibility is required in potential implants, and it can influence cell proliferation and differentiation, and even the longevity of the implant [41]. Live/Dead staining results showed that all four scaffolds had good cytocompatibility in vitro. The rBMMSCs inoculated in the Gxy group had a stronger ability to differentiate into osteoblasts. This may be because the porosity of the Gxy group gradually increases from the center to the periphery, with the larger peripheral porosity in contact with the cells, research indicates that macroporous structures ensure nutrient and metabolic waste transport, vascular ingrowth, and direct osteogenesis [42]. Porous scaffolds with increasing porosity from the center to the periphery have better mechanical strength and superior biocompatibility.

It has been noted that targeted bone tissue regeneration requires biologically active implantable scaffold materials, which are essential for treating bone defects and guiding bone tissue engineering [43]. Numerous studies have demonstrated that rhBMP-2 and porous scaffold composites exhibit osteoinductive activity and osteoconductivity, effectively inducing bone growth into the porous structure and promoting osseointegration [44]. Applications of rhPDGF-BB in bone tissue engineering include peri-implant bone defect repair and guided bone

tissue regeneration [33]. It has been shown that recombinant human platelet-derived growth factor-B chain homodimer (rhPDGF-BB) has a beneficial role in promoting angiogenesis and bone fusion [45].In our experiment, we investigated whether rhBMP-2 and PDGF-BB, either individually or in combination as a bio-coating on composite scaffolds, have an osteogenic effect and the ability to promote osseointegration. The cell proliferation rate in the three types of composite scaffolds was higher than that in the uncoated porous scaffolds, likely due to the increased surface roughness and wettability of the coated scaffolds, which favored cell adhesion and proliferation. The three different composite scaffolds demonstrated better hydrophilicity and biocompatibility than the uncoated porous scaffolds. An important marker of late osteogenic differentiation of rBMMSCs is the formation of calcium nodules by osteoblasts, detectable by alizarin red staining [46]. The B + P group exhibited the highest levels of calcium deposits. However, the difference between the B + P group and the B group was not statistically significant, which may be attributed to the fact that PDGF-BB primarily influences early osteogenesis [47].

According to the results of vivo experiments, micro-CT scanning of the 3D reconstructed images showed new bone tissue growing into the implanted scaffold both on the surface and inside the scaffold at all times of observation. The BV/TV results suggest that the bone volume fraction of all stent repair groups was significantly higher than that of the control group at all periods, which affirms the bone regeneration-promoting effect of growth factors combined with porous scaffolds. At week 4, the new bone formation in group B was greater than in group P (B: 13.28%, P: 11.67%). However, in weeks 8 and 12, the new bone formation in group B and group P showed no significant differences (B: 25.00%, P: 24.88%; B: 32.11%, P: 31.91%). This may be attributed to the stronger burst release effect of BMP-2 compared to PDGF-BB in vivo, leading to a higher initial release rate. Although the authors used chitosan to load BMP-2 for sustained release, they were unable to completely control the early release rate of BMP-2, resulting in a higher concentration of BMP-2 during the early stages, thereby stimulating osteogenesis. The HE staining results of subcutaneous implants and rat organs showed that this concentration of BMP-2 remained within a safe range, without causing adverse effects in the soft tissues or vital organs of the rats. As the healing time progressed, the release rate of BMP-2 was better controlled, and the osteogenic effect became more gradual and stable. The stability of the newly formed bone and the interface between the scaffold and bone was also an important observation index [48]. VG staining revealed that new bone formation occurred on both the surface and inside of the scaffold, with good bone integration at the scaffold-bone interface. Moreover, the new bone and bone integration effects in the B + P group were superior to those in the individual B and P groups, which was consistent with the analysis results from micro-CT scanning.

The limitations of our study are discussed herein. While comprehensive investigations were conducted through histological staining and micro-CT scanning to evaluate the osteogenic effects of various porous and composite scaffolds, certain constraints remain. Most notably, the expression levels of osteogenic genes were not directly validated using polymerase chain reaction (PCR) analysis, creating a gap in our understanding of the molecular mechanisms underlying growth factor-induced osteogenesis. Future studies should incorporate PCR to thoroughly assess osteogenic gene expression and investigate relevant signaling pathways (e.g., TGF-β/BMPs, Wnt, and MAPK) that mediate osteoblast differentiation, thereby elucidating the mechanisms of bone regeneration promotion. Additionally, the optimal ratio of the two growth factors was not systematically examined. Subsequent research should evaluate different growth factor ratios to identify the combination that maximizes bone regeneration while minimizing adverse effects, which would provide critical data for clinical applications. Furthermore, while growth factor coating was performed under aseptic conditions, additional sterilization was omitted to preserve bioactivity, as conventional high-temperature or irradiation methods would degrade the biomolecules. Although contamination risks were minimized, this approach does not meet the stringent sterilization standards required for clinical translation. As emphasized in recent literature [49], biomaterials composed of multiple chemical or bioactive components require carefully designed, stepwise sterilization protocols that ensure both sterility and the preservation of material functionality. Therefore, further research is essential to explore alternative low-temperature sterilization techniques that are compatible with the coated biomolecules. Additionally, it is crucial to evaluate the long-term stability, sterility maintenance, and drug release kinetics of these scaffolds following sterilization. These studies are necessary to bridge the gap between preclinical models and clinical applications, ensuring the material's practical feasibility and safety for human use.

Conclusions

This study systematically compares the properties of porous structures with different gradient orientations. Within a suitable range of porosity and pore size, uniform porous, radial-gradient, and axial-gradient porous structures exhibit comparable mechanical properties. However, radial-gradient porous structures demonstrate superior biocompatibility, making them a promising

candidate for dental implant applications. Subsequently, BMP-2/PDGF-BB-loaded chitosan microspheres were incorporated into the radial-gradient porous scaffolds to form a composite scaffold. The composite scaffold shows low cytotoxicity and effectively enhances cell adhesion, proliferation, and differentiation. 3D-printed porous scaffolds modified with BMP-2 and PDGF-BB-loaded chitosan microspheres promote bone regeneration and facilitate bone defect repair. Notably, BMP-2 exhibits osteogenic potential comparable to PDGF-BB in vivo. Moreover, titanium scaffolds co-modified with BMP-2 and PDGF-BB demonstrate superior osteogenic capacity compared to scaffolds modified with either factor alone, indicating a synergistic effect of BMP-2 and PDGF-BB in promoting bone formation in vivo.

Abbreviations

3D	Three-dimensional
Ti	titanium
rhBMP-2	Recombinant human bone morphogenetic protein-2
PDGF-BB	Platelet Derived Growth Factor
FEA	Finite element analysis
SLM	Selective laser melting
SD Rat	Sprague–Dawley Rat
CCK-8	Cell counting kit-8
OD	Optical Density
ALP	Alkaline phosphatase
Micro-CT	Micro Computed Tomography
SLM	Selective laser melting
CBCT	Cone Beam Computed Tomography
BMPs	Bone morphogenetic protein
BMP-2	Bone Morphogenetic Protein-2
TPMS	The bone morphogenetic protein-2
TPMS	Three-period minimal surface structure
rBMMSCs	Rat bone marrow mesenchymal stem cells
GPa	Gigapascal
UM	Micro
N	Newtons
TPP	Sodium Triphosphate
BCIP/NBT kit	alkaline phosphatase colorimetric kit
HE	Hematoxylin home hematoxylin and eosin
BV	Bone volume
TV	Total volume
PFA	Paraformaldehyde
FAA	Formaldehyde-acetic acid-alcohol
PCR	Polymerase chain reaction

Supplementary Information

The online version contains supplementary material available at https://doi.org/10.1186/s12903-025-06110-2.

Supplementary Material 1

Acknowledgements

The authors would like to thank shiyanjia lab (www.shiyanjia.com) for the support of SEM test.

Author contributions

Conceptualization, B.W.; methodology, D.C., C.W., G.G. and H.D.; software, D.C. and G.G.; validation, S.Z., S.X., J.L., C.W. and Q.Z.; formal analysis, C.J.,S.S., G.G. and H.D.; investigation, S.S., H.D., G.G. and C.J.; resources, B.W.; data curation, G.G.,S.Z., and S.X.; writing—original draft preparation, C.J. and S.X.; writing—review and editing, C.J., S.X., S.Z., G.G., and B.W.; visualization, C.J.; supervision, B.W.; project administration, W.B.; funding acquisition, B.W. All authors have read and agreed to the published version of the manuscript.

Funding

This research was supported by the National Natural Science Foundation of China (82060208).

Data availability

The datasets used or analyzed during the current study are available from the corresponding author upon reasonable request.

Declarations

Institutional review board statement

The experiment was approved by the Experimental Animal Welfare Ethics Committee of the First Affiliated Hospital of Nanchang University (ethical approval number: CDYFY-IACUC-202308QR025). We obtained informed consent from the owners of the animals for the use of these animals in the study. All methods were carried out following relevant guidelines and regulations.

Consent for publication

Not Applicable.

Competing interests

The authors declare no competing interests.

Author details

[1]Department of Stomatology, The First Affiliated Hospital of Nanchang University, Nanchang, Jiangxi 330000, China
[2]Department of Stomatology, The Affiliated Stomatological Hospital of Jiujiang University, Jiujiang, Jiangxi 332000, China
[3]Department of Stomatology, The Fifth Hospital of Xiamen, Xiamen 361000, China
[4]Department of Stomatology, Jiangxi Provincial People's Hospital, Nanchang, Jiangxi 330000, China
[5]Department of Stomatology, Shanghai Pudong Hospital, Shanghai 200135, China

Received: 28 November 2024 / Accepted: 5 May 2025
Published online: 27 May 2025

References

1. Barba D, Alabort E. and R.C.J.A.b. Reed, Synthetic Bone: Design by Additive Manufacturing. 2019.
2. B BZA et al. Bio-surface coated titanium scaffolds with cancellous bone-like biomimetic structure for enhanced bone tissue regeneration - ScienceDirect. 2020;114:431–48.
3. Giannitelli SM et al. Current trends in the design of scaffolds for computer-aided tissue engineering. 2014;10(2):580–594.
4. Gómez S, et al. Design and properties of 3D scaffolds for bone tissue engineering. Acta Biomater. 2016;42:341–50.
5. Annur D et al. Titanium and titanium based alloy prepared by spark plasma sintering method for biomedical implant application-A review. 2021.
6. Sibiryakov B, Leite LWB, J.J.o.A E. Porosity Specif Surf Area Permeability Porous Media. 2021;186(5):104261.
7. Kelly CN et al. Fatigue behavior of As-built selective laser melted titanium scaffolds with sheet-based gyroid microarchitecture for bone tissue engineering. 2019;94:610–626.
8. Jiao J, et al. Influence of porosity on osteogenesis, bone growth and osteointegration in trabecular tantalum scaffolds fabricated by additive manufacturing. Front Bioeng Biotechnol. 2023;11:1117954.
9. Yang Y, et al. Gaussian curvature-driven direction of cell fate toward osteogenesis with triply periodic minimal surface scaffolds. Proc Natl Acad Sci U S A. 2022;119(41):e2206684119.
10. Ma Z et al. Lattice structures of Cu-Cr-Zr copper alloy by selective laser melting: microstructures, mechanical properties and energy absorption. 2019;187:108406.

11. Pei X et al. 3D printed titanium scaffolds with homogeneous diamond-like structures mimicking that of the osteocyte microenvironment and its bone regeneration study. Biofabrication, 2020;13(1).
12. Dziaduszewska M, Materials AZJ. Structural and Material Determinants Influencing the Behavior of Porous Ti and Its Alloys Made by Additive Manufacturing Techniques for Biomedical Applications. 2021(4).
13. Kelly CN, et al. Fatigue behavior of As-built selective laser melted titanium scaffolds with sheet-based gyroid microarchitecture for bone tissue engineering. Acta Biomater. 2019;94:610–26.
14. Mitra I, et al. 3D printing in alloy design to improve biocompatibility in metallic implants. Mater Today (Kidlington). 2021;45:20–34.
15. Zhang P et al. Ti-Based biomedical material modified with TiO(x)/TiN(x) duplex bioactivity film via Micro-Arc oxidation and nitrogen ion implantation. Nanomaterials (Basel), 2017;7(10).
16. Ziqiang et al. Enhanced loading and controlled release of rhBMP-2 in thin mineralized collagen coatings with the aid of chitosan nanospheres and its biological evaluations. 2014;2(28):4572–4582.
17. Muthu M et al. A Review on the Antimicrobial Activity of Chitosan Microspheres: Milestones Achieved and Miles to Go. 2023;11(8).
18. Komatsu K, et al. Platelet-derived growth factor-BB regenerates functional periodontal ligament in the tooth replantation. Sci Rep. 2022;12(1):3223.
19. Yoshida S et al. PDGFBB promotes PDGFRα-positive cell migration into artificial bone in vivo. 2012;421(4):785–9.
20. Suárez-López D, Amo F, Monje A. Efficacy of biologics for alveolar ridge preservation/reconstruction and implant site development: an American academy of periodontology best evidence systematic review. J Periodontol. 2022;93(12):1827–47.
21. Kim SE, et al. Co-delivery of platelet-derived growth factor (PDGF-BB) and bone morphogenic protein (BMP-2) coated onto heparinized titanium for improving osteoblast function and osteointegration. J Tissue Eng Regen Med. 2015;9(12):E219–28.
22. Chang YC, et al. Surface analysis of titanium biological modification with glow discharge. Clin Implant Dent Relat Res. 2015;17(3):469–75.
23. Shehriar H, et al. Chitosan Biomaterials Curr Potential Dent Appl. 2017;10(6):602.
24. Tao X et al. Synthesis pH Glucose Responsive Silk Fibroin Hydrogels 2021. 22(13).
25. Bayer EA, et al. (*) programmed Platelet-Derived growth Factor-BB and bone morphogenetic Protein-2 delivery from a hybrid calcium phosphate/alginate scaffold. Tissue Eng Part A. 2017;23(23–24):1382–93.
26. Cruz RS, et al. Biomechanical influence of narrow-diameter implants placed at the crestal and subcrestal level in the maxillary anterior region. A 3D finite element analysis. J Prosthodont. 2024;33(2):180–7.
27. Hou C, et al. Additive manufacturing of functionally graded porous titanium scaffolds for dental applications. Biomater Adv. 2022;139:213018.
28. Liu H, et al. D-mannose attenuates bone loss in mice via Treg cell proliferation and gut microbiota-dependent anti-inflammatory effects. Ther Adv Chronic Dis. 2020;11:2040622320912661.
29. Melancon D, et al. Mechanical characterization of structurally porous biomaterials built via additive manufacturing: experiments, predictive models, and design maps for load-bearing bone replacement implants. Acta Biomater. 2017;63:350–68.
30. Liu C, et al. Circular RNA AFF4 modulates osteogenic differentiation in BMMSCs by activating SMAD1/5 pathway through miR-135a-5p/FNDC5/Irisin axis. Cell Death Dis. 2021;12(7):631.
31. Smeets R, et al. Impact of dental implant surface modifications on osseointegration. Biomed Res Int. 2016;2016:p6285620.
32. Arabnejad S et al. High-strength porous biomaterials for bone replacement: A strategy to assess the interplay between cell morphology, mechanical properties, bone ingrowth and manufacturing constraints. 2016;30(8):345–56.
33. Majhy B, Priyadarshini P, Sen AK. Effect of surface energy and roughness on cell adhesion and growth - facile surface modification for enhanced cell culture. RSC Adv. 2021;11(25):15467–76.
34. Lee MC et al. Design, manufacture, and characterization of a Critical-Sized gradient porosity Dual-Material tibial defect scaffold. Bioeng (Basel), 2024. 11(4).
35. Li L, et al. Design of a Haversian system-like gradient porous scaffold based on triply periodic minimal surfaces for promoting bone regeneration. J Adv Res. 2023;54:89–104.
36. Gao C, et al. Bone Biomaterials Interact Stem Cells. 2017;5(4):17059.
37. Turnbull G et al. 3D bioactive composite scaffolds for bone tissue engineering. 2017(3).
38. Sola A, Bellucci D, Cannillo V. Functionally graded materials for orthopedic applications - an update on design and manufacturing. Biotechnol Adv. 2016;34(5):504–31.
39. Vaquette C, et al. Resorbable additively manufactured scaffold imparts dimensional stability to extraskeletally regenerated bone. Biomaterials. 2021;269:120671.
40. Mokhtari-Jafari F, Amoabediny G, Dehghan MM. Role of biomechanics in vascularization of tissue-engineered bones. J Biomech. 2020;110:109920.
41. Lai M, Jin Z, Su Z. Surface modification of TiO(2) nanotubes with osteogenic growth peptide to enhance osteoblast differentiation. Mater Sci Eng C Mater Biol Appl. 2017;73:490–7.
42. Zhou J, et al. Study on the influence of scaffold morphology and structure on osteogenic performance. Front Bioeng Biotechnol. 2023;11:1127162.
43. Kim MJ et al. BMP-2-immobilized PCL 3D printing scaffold with a leaf-stacked structure as a physically and biologically activated bone graft. Biofabrication, 2024;16(2).
44. Uribe F, et al. Comparison of rhBMP-2 in combination with different biomaterials for regeneration in rat calvaria Critical-Size defects. Biomed Res Int. 2022;2022:p6281641.
45. Nayak VV, et al. A rhPDGF-BB/bovine type I collagen/β-TCP mixture for the treatment of critically sized non-union tibial defects: an in vivo study in rabbits. J Orthop Res. 2024;42(9):1998–2006.
46. Bernar A et al. Optimization of the Alizarin red S assay by enhancing mineralization of osteoblasts. Int J Mol Sci, 2022;24(1).
47. Wang F, et al. PDGFR in PDGF-BB/PDGFR signaling pathway does orchestrates osteogenesis in a Temporal manner. Res (Wash D C). 2023;6:0086.
48. Sparks DS, et al. Convergence of scaffold-guided bone regeneration principles and microvascular tissue transfer surgery. Sci Adv. 2023;9(18):eadd6071.
49. Kunrath MF, Shah FA, Dahlin C. Bench-to-bedside: feasibility of nano-engineered and drug-delivery biomaterials for bone-anchored implants and periodontal applications. Mater Today Bio, 2023;18.

Publisher's note